Japanese Journal of Applied Physics

REGULAR PAPER

Impact of PTFE particle size in designing $BaTiO_3$ dielectric composites under the cold sintering process

To cite this article: Takashi Nunokawa *et al* 2023 *Jpn. J. Appl. Phys.* **62** 071003

Japanese Journal of Applied Physics **62**, 071003 (2023) **REGULAR PAPER**
https://doi.org/**10.35848/1347-4065/ace145**

Impact of PTFE particle size in designing $BaTiO_3$ dielectric composites under the cold sintering process

Takashi Nunokawa[1,2*], Kenji Takashima[1], Kotaro Mizuno[1], and Clive A. Randall[2,3*]

[1]*R&D Center, TAIYO YUDEN CO., Ltd., Takasaki, Gunma 370-3347, Japan*
[2]*Materials Research Institute, The Pennsylvania State University, University Park, PA 16802, United States of America*
[3]*Department of Materials Science and Engineering, The Pennsylvania State University, University Park, PA 16802, United States of America*

[*]E-mail: tpn5173@psu.edu; car4@psu.edu

Received February 22, 2023; revised May 31, 2023; accepted June 22, 2023; published online July 18, 2023

The Cold Sintering Process (CSP) can provide opportunities to fabricate high-performance $BaTiO_3$ dielectric composites with polymer materials that are typically difficult to impossible to co-process under a conventional sintering process. Therefore, we investigated the preparation process of $BaTiO_3$ sintered body by CSP and integrated a well-dispersed intergranular polymer phase. In this study, we focused on preparing $BaTiO_3$ and Polytetrafluoroethylene (PTFE) composites. We considered the importance of the particle size of the PTFE phase, and correlated the impact on the composite dielectric properties. Through fitting a general-mixing-law to the dielectric properties as a function of volume fraction, we could deduce more homogeneous composites obtained in using the 200 nm PTFE powders. In addition, the temperature dependent dielectric properties and field dependent conductivity of the composites was investigated. It was found that with the good dispersion of the PTFE can suppress the leakage current density in the dielectric composites.

1. Introduction

The Cold Sintering Process (CSP) has attracted much attention because of the ability to densify at low temperatures between 100 °C to 300 °C for a number of important functional ceramics such as $BaTiO_3$,[1–5] ZnO,[6–11] V_2O_5,[12–14] SnO,[15] Li_2MoO_4,[16,17] $Li_{1.5}Al_{0.5}Ge_{1.5}(PO_4)_3$ (LAGP),[18–20] $Li_{1.3}Al_{0.3}Ti_{1.7}(PO_4)_3$ (LATP),[20] and β-alumina,[21] and (K, Na)NbO_3 (KNN).[22–24] Under conventional sintering conditions, these ceramics must be densified at significantly higher temperatures, so one major interest is the potential that CSP can provide an alternative route to a sustainable production process.

The CSP is a non-equilibrium thermodynamic sintering process that uses a chemo- mechanical mechanism known as pressure solution creep. This drives a critical series of mechanisms such as dissolution, grain boundary transport, and precipitation to densify the particulates into a densified ceramic. Pressure solution creep is known from a geological process enabling sedimentary rock formation. In that case, the particulate densification process takes hundreds of thousands of years.[25–27] With CSP, we consider material selection, uni-axial pressures, transient chemistries, low temperatures, and smaller particle sizes that densification can be a faster process and therefore a possible manufacturing route. By adding the appropriate transient fluxes, such as an acid or base chelating agents, the chemo- mechanical activated dissolution, diffusion, and precipitation process. These can all occur at the interfaces of the contacting particles that are under an applied stress.[28] This takes place in an open system, whereupon volatile components of the flux can escape from the gaps between the die walls and pressing plungers.[3]

Being able to effectively drive the diffusional process for densification at low temperatures, we can fabricate metastable materials and combine different materials together to form unique composites. Ceramics, metals, polymers, and 2D materials have all been co-sintered into dense monolithic and multilayer structures under CSP.[29–31] Therefore, CSP permits a universal approach to integrate all materials provided the appropriate transient phase can be found to permit the pressure solution creep to be activated with sufficient kinetics.

$BaTiO_3$ is an important dielectric ceramic material that is a ferroelectric. It has a high permittivity and is extremely important for Multilayer Ceramic Capacitor (MLCC) components. $BaTiO_3$ has a phase transition between a paraelectric phase that is cubic and macroscopically non-polar with symmetry $Pm3m$. At a transition temperature T_c 125 °C, there is a phase transition to a tetragonal ferroelectric phase ($P4mm$). At lower temperatures, there are additional polymorphic phase transitions to a ferroelectric orthorhombic ($Amm2$), and then to a rhombohedral ferroelectric phase ($R3m$). There are dielectric property anomalies that follow a Curie law temperature dependence at each of these phase transitions, and these provide an overall high permittivity across a broad temperature range.[32–34] Under conventional sintering, $BaTiO_3$ requires temperatures ~1200 °C to undergo densification. The relative permittivity magnitude of $BaTiO_3$ ceramics is also very dependent on the grain size, porosity, and crystallinity. The $BaTiO_3$ ferroelectric size effect phenomenon, involves a dilution of the relative permittivity at RT and at the Curie points as the average grain size reduces to below 1.0 micron.[34–36]

As already pointed out, $BaTiO_3$ is most important dielectric for MLCCs. The devices over 4 trillion are fabricated every year. MLCCs are important passive component devices which are constructed with large number of layers. The layers up to 1000 are fabricated in state-of-the-art components. To improve temperature dependence, resistivity, dielectric losses, and the reliability, various dopants are formulated into the dielectric. Mn and Mg as acceptor dopants and rare Earth (Dy, Ho, Er, and Y) as acceptors and donors are added to $BaTiO_3$ in the common base metal MLCCs.[37,38] As an alternative strategy for improving reliability, temperature dependence, and other dielectric properties, we have considered sintering of $BaTiO_3$ mixed with polymers by using CSP.

Typically, as $BaTiO_3$ particles are added to polymers, it is extremely difficult to have high volume fractions of $BaTiO_3$,

and the low permittivity of the polymer significantly suppresses the overall relative permittivity of the composite. The composites including around 40 vol% polymer volume fractions has relative permittivity $\varepsilon_r \sim 30$–80.[39–41] With cold sintering $BaTiO_3$-composites with polymers such as PTFE[3,4] and PPO (Poly(p-phenylene oxide)[5] dense composites can be obtained. These have the potential to have high-relative permittivity, low loss, broad temperature dependences, and reduced non-linearities in terms of voltage saturation, electrical conduction and has the potential to limit oxygen vacancy migration that could aid reliability and breakdown. So, although cold sintering technology is in its infancy, the concept of a nanometer polymer integrated into the grain boundaries modifying the overall electric field distribution. This is attractive for a number of technical reasons including higher field electrostatic energy density, high-voltage operation and elimination of the expensive rare Earth dopants, particularly for large sized MLCCs.

In this study, we target the CSP preparation of $BaTiO_3$-PTFE composites with 3 μm and 200 nm PTFE powders to understand strategies for better dispersion of the polymers in the $BaTiO_3$ grain boundaries. We characterized the uniformity of $BaTiO_3$-PTFE with the aid of mixing law analysis from the relative permittivity of $BaTiO_3$-PTFE composites at RT. These composites are also characterized with respect to dc conductivity.

2. Experimental methods

2.1. Powder characteristics

2.1.1. Preparation of materials. $BaTiO_3$ powders (particle size: 100 nm, BET surface area:10.55 $m^2\,g^{-1}$, Ba/Ti ratio = 1.00) were synthesized by an oxalate method.[42,43] The $BaTiO_3$ powder was first annealed at 700 °C for 1 h to remove organic residues and carbonates from the powder surface [Fig. 1(a)]. Barium hydroxide octahydrate [$Ba(OH)_2{\cdot}8H_2O$] as flux was purchased from Alfa Aesar [Fig. 1(b)]. A $D_{50} \sim 3$ μm PTFE was purchased from Howard Piano Industry [Fig. 1(c)], a $D_{50} \sim 200$ nm PTFE was purchased from Nano Chemazone [Fig. 1(d)].

2.2. CSP

2.2.1. Cold sintered $BaTiO_3$ ceramics. The basic experimental procedure for the CSP of $BaTiO_3$ using $Ba(OH)_2{\cdot}8H_2O$ transient flux is outlined schematically in Fig. 2. The $BaTiO_3$ powder was homogeneously mixed with the transient flux $Ba(OH)_2{\cdot}8H_2O$ by using a pestle and mortar under a N_2 atmosphere to prevent $Ba(OH)_2{\cdot}8H_2O$ from reacting with ambient CO_2. The weight ratio of $Ba(OH)_2{\cdot}8H_2O$ to $BaTiO_3$ was 16.7 wt%. The mixed powder was poured in the die and then compacted under a uni-axially pressure at 350 MPa. The die is first preheated at 80 °C for 30 min under the pressing condition. Next, it was heated up to 225 °C for 1 h still under a constant pressure of 350 MPa. After the dies were cooled down to RT, the samples were taken out. All the samples prepared by CSP process was dried at 200 °C for 24 h under a vacuum oven. The shape of the prepared sample was cylindrical pellet. The diameter was half inch (12.7 mm) and the thickness was about 1.2 mm.

2.2.2. $BaTiO_3$-PTFE composites. $BaTiO_3$ powders are first mixed with PTFE powders by using Thinky mixer. After that, the combined powders were further mixed in ethanol by using a pestle and mortar until the ethanol was evaporated. The ratios of PTFE to $BaTiO_3$ were 5, 10, and 20 vol%. This powder was further modified with the addition of the transient flux chemistry, where 16.7 wt% $Ba(OH)_2{\cdot}8H_2O$ was added and then homogeneously mixed by using mortar and pestle under an N_2 atmosphere. The mixed powders were then cold sintered under a uni-axial pressure of 350 MPa at 225 °C for 2 h.

2.2.3. Material characterization. Bulk densities (ρ_b) were obtained as sintered pellets by the geometric method. Theoretical densities (ρ_{th}) were considered for pure $BaTiO_3$ (6.03 g cm^{-3}) and 0.95 $BaTiO_3$−0.05 PTFE composites

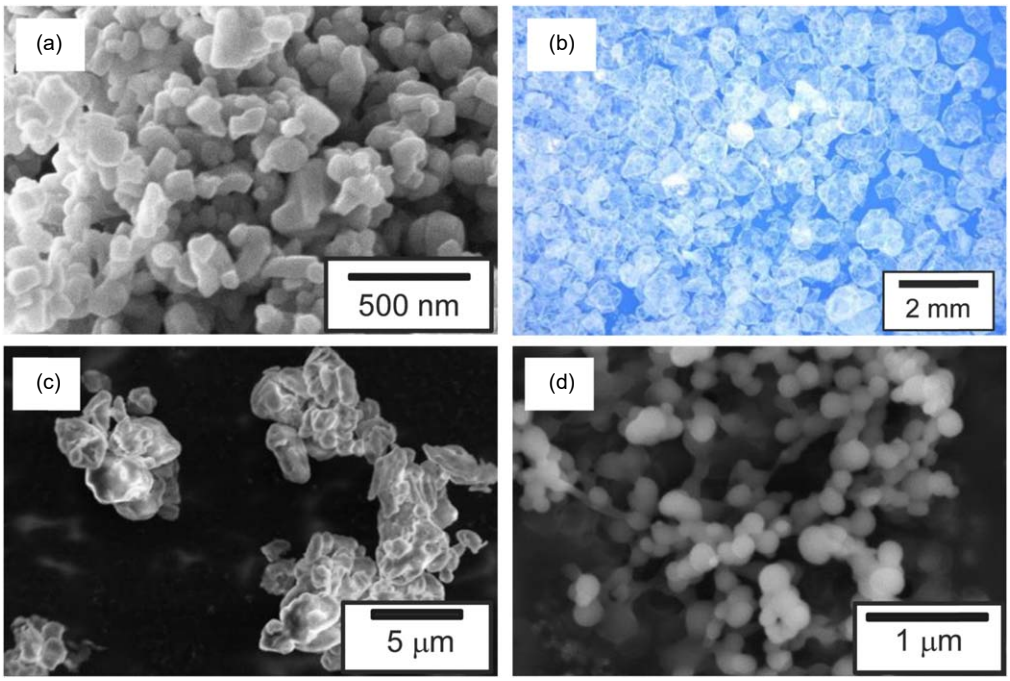

Fig. 1. SEM image of the calcined $BaTiO_3$ synthesized by the oxalate method[42,43] (a), optical image of $Ba(OH)_2{\cdot}8H_2O$ purchased from Alfa Aesar (b), SEM image of the 3 μm PTFE purchased from Howard Piano Industry (c) and SEM image of the 200 nm PTFE purchased from Nano Chemazone (d).

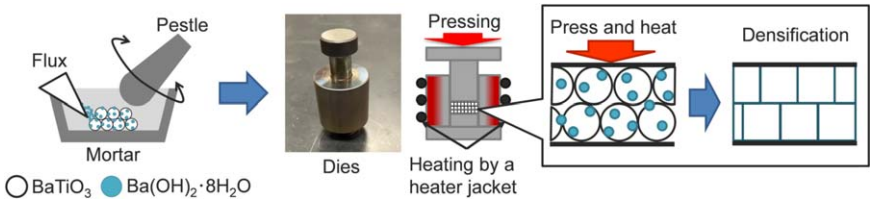

Fig. 2. Schematic illustration of experimental procedures and setup for cold sintering of $BaTiO_3$ using $Ba(OH)_2 \cdot 8H_2O$ flux.

(5.83 g cm^{-3}). The relative density was then calculated from the ρ_b/ρ_{th} ratio.

X-ray diffraction (XRD) was measured at 45 kV and 40 mA with Cu-Kα radiation (Empyrean, Malvern Pananalytical). Diffraction patterns were collected at 2θ angles between 10° and 90° with a step size of 0.026° and a scan rate of 0.067° s^{-1}. Scanning electron microscopy (SEM) images were observed using fracture surfaces of the samples under an accelerating voltage of 5 kV (Apreo SEM, Thermo Scientific).

For the electrical property characterization, 100 nm thick Pt electrodes were deposited by sputtering (Q150R Plus, Quorum Technologies) on the polished surfaces. Temperature properties were measured at 1 MHz and 1$_{VRMS}$ in the temperature range between 25 °C and 200 °C using LCR meter (E4980A, Agilent Technologies). Current–voltage (*I–V*) measurements were measured by using HP 4140B pA meter with Trek Model 610D high-voltage amplifier system. We calculated current density–electric field (*J–E*) and the resistivity from the results of *I–V* measurements and considering the sample thickness and electrode size.

3. Results and discussion

3.1. Material characterizations

Figure 3 shows relative density of $BaTiO_3$-PTFE composites as function of the volume fraction PTFE. The composites all have ~90% relative density and above. Figure 4 shows the XRD pattern for scans from 20 to 80 degrees for important examples of the different process stages. This includes the annealed $BaTiO_3$ before CSP, the cold sintered $BaTiO_3$, the $BaTiO_3$ with 3 μm PTFE powders at 5 vol% and $BaTiO_3$ with 200 nm powders of PTFE with 5 vol% content all having undergone the densification with CSP. We observed single spectrum in 200 and 002 reflections. In the results of a Rietveld analysis, *c/a* of the calcined $BaTiO_3$, the cold sintered $BaTiO_3$, the $BaTiO_3$-3 μm PTFE 5 vol% and the $BaTiO_3$-200 nm PTFE 5 vol% were 1.0054, 1.0051, 1.0044, and 1.0042, respectively. As each value

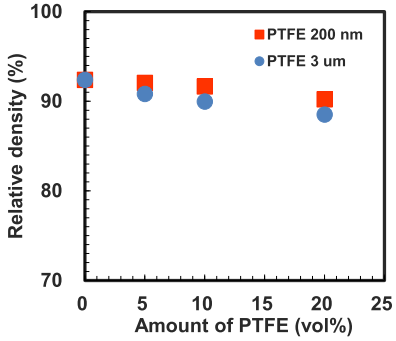

Fig. 3. Relative density of the $BaTiO_3$-PTFE composites as function of the amount of PTFE.

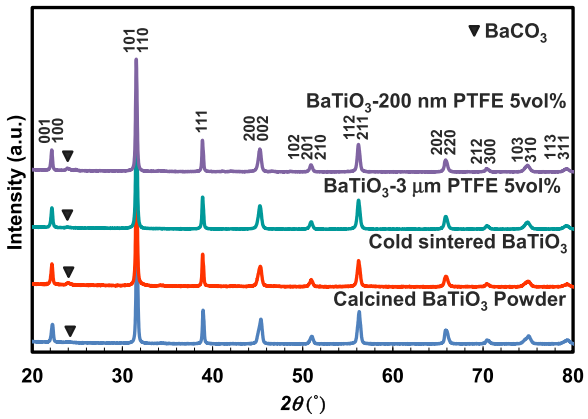

Fig. 4. XRD patterns of the calcined $BaTiO_3$ before CSP, the cold sintered $BaTiO_3$, the $BaTiO_3$-3 μm PTFE 5 vol% and the $BaTiO_3$-200 nm $BaTiO_3$ 5 vol% after CSP.

of *c/a* was more than 1, it is indicated that these are ferroelectric $BaTiO_3$ being used for CSP as it has a tetragonal structure. Two peaks of 200 and 002 reflections are overlapped because the two peaks are close and typically seen in nano-$BaTiO_3$. There was a small detectable peak associated with the presence of a $BaCO_3$ phase in all cases. We quantified the amount of $BaCO_3$ in the samples with a Rietveld analysis. Amount of $BaCO_3$ in the calcined $BaTiO_3$ before CSP was 1.5 wt%. On the other hand, cold sintered $BaTiO_3$, $BaTiO_3$-3 μm PTFE 5 vol% and $BaTiO_3$-200 nm PTFE 5 vol% slightly increases with 3.2 wt%, 2.8 wt%, and 3.8 wt% respectively. So, under the CSP the $BaCO_3$ was slightly increased from 1 to 2 wt%. We believe that the $Ba(OH)_2 \cdot 8H_2O$ partially reacts with ambient CO_2 during CSP.

Figures 5(a-1) and 5(a-2) show the microstructure with a series of SEM images of the cold sintered $BaTiO_3$. The $BaTiO_3$ pellets densified by CSP were obtained with faceted shaped $BaTiO_3$ grains and these having been evolved from the more spherical $BaTiO_3$ starting powder morphologies. Faceted grains evolution is an important indicator of the sintering process under cold sintering and can be explained in terms of size and densification rates within the pressure solution creep models, as outlined recently by Ndayishimiye et al.[27] Figures 5(b-1) and 5(b-2) show SEM images of the microstructures of $BaTiO_3$-3 μm PTFE 5 vol%, and with Figs. 5(c-1) and 5(c-2) show SEM images of the microstructures of $BaTiO_3$-200 nm PTFE 5 vol%. As highlighted with white arrows, fiber-like substances were observed in the cross-sections of the $BaTiO_3$-PTFE composites. The substances were found irrespective of PTFE particle size. These are associated with heterogeneous localized PTFE phases throughout the microstructure.

3.2. Electrical characterizations

Figure 6 shows temperature dependence of the relative permittivity and the dielectric loss, measured at 1 V$_{RMS}$

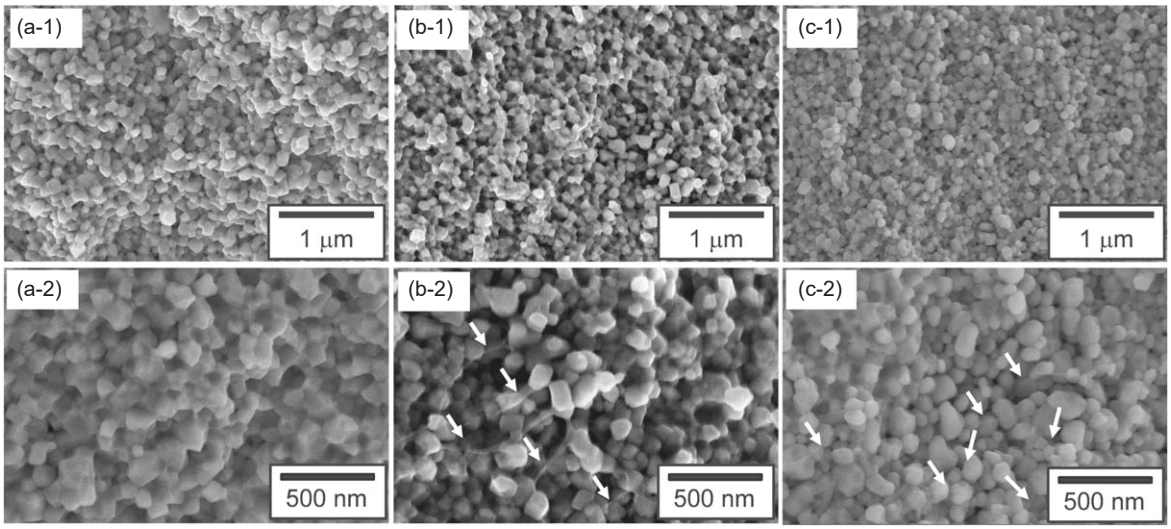

Fig. 5. SEM images of the cold sintered $BaTiO_3$ [(a-1): low magnification, (a-2): high magnification], the $BaTiO_3$-3 μm PTFE 5 vol% [(b-1): low magnification, (b-2): high magnification], and the $BaTiO_3$-200 nm PTFE 5 vol% [(c-1): low magnification, (c-2): high magnification].

and 1 MHz, of the cold sintered $BaTiO_3$ over a temperature range from 25 °C to 200 °C. The relative permittivity and the dielectric loss at RT were 1580 and 0.11, respectively. There is a relative permittivity maximum at a $T_c \sim 125$ °C associated with the ferroelectric–paraelectric phase transition of the $BaTiO_3$. The relative permittivity is ~3000 at the peak. It was noted that the cold sintered $BaTiO_3$ had a relatively high permittivity over the temperature range for a $BaTiO_3$ with a grain size of 100 nm. However, these dielectrics have a higher dielectric loss than a conventional sintered $BaTiO_3$. This is associated with the residual hydroxides from the decomposition of the transient phase, $Ba(OH)_2{\cdot}8(H_2O)$. From grain growth perspective, the particle size and the distribution in the calcined $BaTiO_3$ before CSP were 109.5 ± 26.3 nm. The grain size and the distribution after CSP were almost the same as those of the initial powders. The broadening of the dielectric temperature curves could be influenced by size effect of $BaTiO_3$. Other authors have also reported that the dielectric temperature dependence can broaden as the grain size decreases owing to low permittivity interfaces in grain boundaries.[44–46)]

To contrast with the pure ceramic cold sintered $BaTiO_3$, we measured the temperature dependence of the relative permittivity and the dielectric loss of $BaTiO_3$-PTFE composites. We note that there is a systematic dilution of the relative permittivity, a suppression of the dielectric anomaly that leads to flattened temperature dependences, and improvement in the dielectric losses. Figures 7(a) and 7(b) show these trends in the relative permittivity of $BaTiO_3$-3 μm PTFE and $BaTiO_3$-200 nm PTFE. Figures 7(c) and 7(d) show the temperature dependence of the dielectric loss of $BaTiO_3$-3 μm PTFE and $BaTiO_3$-200 nm PTFE, respectively. There is a significant difference within the same volume fractions, contrasting the starting materials with particle sizes of 3 μm and 200 nm. The RT permittivity of these composites in both cases still are much higher than $BaTiO_3$ polymer composites previously fabricated with a process except for the CSP.[39–41)] The importance of the powder size is linked with the dispersion of the PTFE. To analyze this important observation, we need to investigate in detail with the aid of a mixing law analysis.

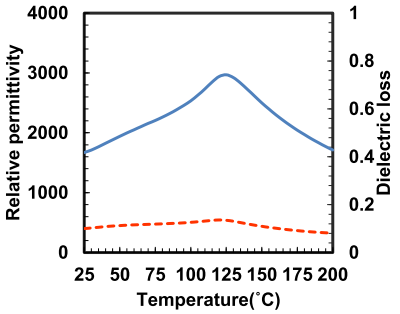

Fig. 6. Temperature dependence of the relative permittivity and the dielectric loss, measured at 1 V_{RMS} and 1 MHz, of the cold sintered $BaTiO_3$.

Figure 8 shows the relative permittivity at RT as function of PTFE volume fraction in the $BaTiO_3$-PTFE composites. As the PTFE volume fraction was increased, the relative permittivity of the $BaTiO_3$-PTFE is systematically decreased. The variation was analyzed with the RT relative dielectric permittivity and found to follow the logarithmic law, which is the limiting case of $n -> 0$ of the general mixing law.[47–50)] The general mixing law for N constituent phases in a composite is given by:

$$\bar{\varepsilon}_r^n = \sum_{i=1}^{N} f_i \varepsilon_i^x, \tag{1}$$

where is the average relative permittivity, f_i is the relative volume fraction of the ith phase, ε_i is the relative permittivity of the ith phase, and n is the exponent, $-1 \leqslant n \leqslant +1$. The exponent, n, is influenced by the spatial connectivity of each of the phases, as at the extremes: $n = +1$ is the parallel connectivity, $n = -1$ is the serial connectivity, and $n = 0$ is an equal weighted mixture of parallel and serial connectivity. The $BaTiO_3$-3 μm PTFE and $BaTiO_3$-200 nm gave exponents of $n = -0.4$ and -0.18, respectively from the general mixing law, as shown in Fig. 8. In brief, PTFE in the $BaTiO_3$-200 nm PTFE is more mixed and spatially dispersed than that of $BaTiO_3$-3 μm PTFE, because 200 nm PTFE is finer than 3 μm PTFE. In a similar study, Sada et al.[4)] was able to prepare $BaTiO_3$-PTFE composites given $n = -0.24$ under the general mixing law. Therefore, the push towards an ideal

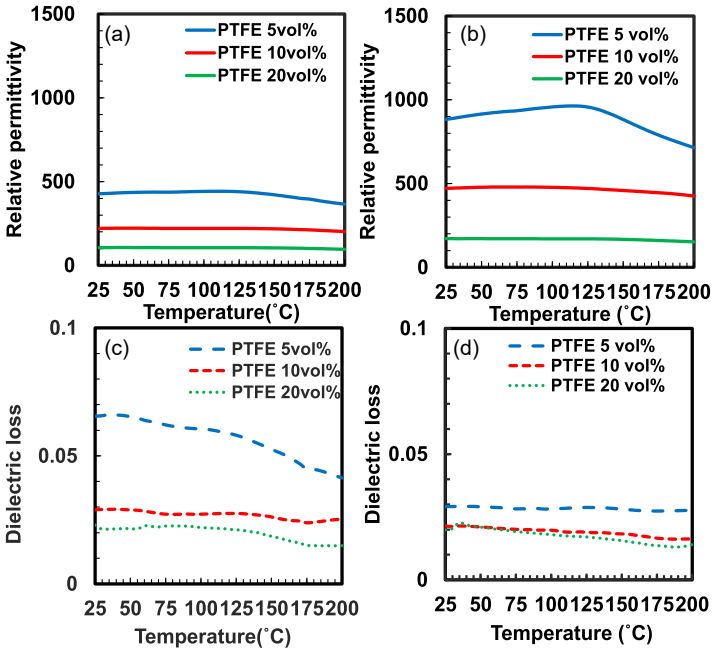

Fig. 7. Temperature dependence of the relative permittivity of the $BaTiO_3$-3 μm PTFE (a) and $BaTiO_3$-200 nm PTFE (b), and the dielectric loss of the $BaTiO_3$-3 μm PTFE (c) and the $BaTiO_3$-200 nm PTFE (d).

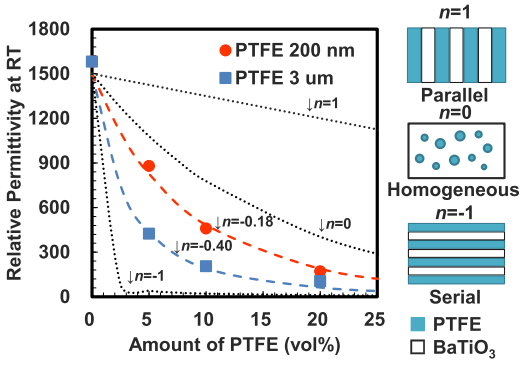

Fig. 8. Systematic variation of the RT relative permittivity, with the dotted line being the mixing law with $n = +1, 0, -1$. Schematic illustration of connectivity patterns at given n is shown on the right side.

dispersion of nanoscale polymers around each $BaTiO_3$ grain boundary requires the dispersion of finer PTFE powders in the $BaTiO_3$. Also, we have improved a series of dilutions on the overall permittivity to $n = -0.18$. For the dispersion of polymer in the grain boundaries of a ceramic, the limiting and ideal case will have $n = 0$. Furthermore, the temperature dependence of the permittivity is improved with the addition of PTFE. Also, the dielectric loss is significantly improved with the PTFE. The best dielectric trends are shown with the better dispersed PTFE powder. On the other hand, the exponents n of 3 μm PTFE and 200 nm PTFE was -0.44 and -0.30 respectively at Curie temperature. The exponents of this temperature are sufficiently away from that of the RT. The phase transition region is more complexed and less reliable to model the connectivity.

In addition to relative permittivity, resistivity is also one of the great important properties. To determine the resistivity, we performed I–V measurements with the data normalized with the geometry of the samples and plotted in terms of current density, J, and average electric field strength, E. Figure 9(a) shows J–E curve of cold sintered $BaTiO_3$, $BaTiO_3$-3 μm PTFE 5 vol% and $BaTiO_3$-200 nm PTFE 5 vol%. The leakage current density of the cold sintered $BaTiO_3$ was the highest, and there is a non-Ohmic increase in current density at high fields. The leakage current density has substantially decreased by adding PTFE and there is an Ohmic dependence as a function of the applied field. Contrasting the data in the form of a Fowler–Nordheim[51–53] plot, Fig. 9(b) suggests that as

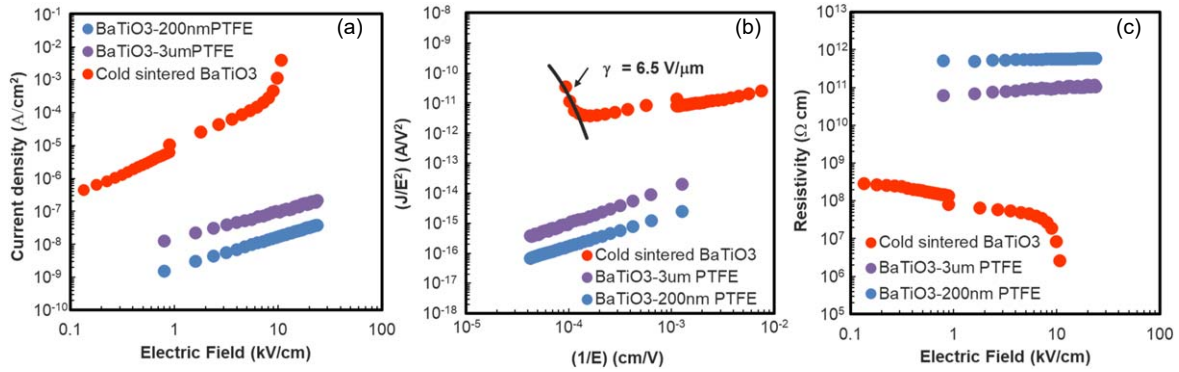

Fig. 9. J–E curve of the cold sintered $BaTiO_3$ and the $BaTiO_3$-PTFE 5 vol% composites (a), a Fowler–Nordheim plot of these materials (b), and the resistivity of the cold sintered $BaTiO_3$ and the $BaTiO_3$-PTFE composites as function of the electric field (c).

increasing the field in the cold sintered samples there is a loss of resistance in the form of a tunneling mechanism. Fowler–Nordheim plots are an effective methodology to separate field-dependent conduction phenomenon in semiconductor materials and devices. We note that at high fields, *E,* the data follows the tunneling dependence of the current density, *J* with *A* and γ as constants given by the equation:

$$J = AE^2 \exp\left[\frac{-\gamma}{E}\right]. \quad (2)$$

In the cold sintered $BaTiO_3$, the γ equaled 6.5 V μm^{-1}. It was found that the leakage current density with the polymers suppressed this tunneling and much greater dc field could be applied.

With the better dispersion of $BaTiO_3$-200 nm powders with 5 vol% PTFE, compared to the $BaTiO_3$-3 μm powder, finer PTFE also reflects in further improvement of the resistivity. Figure 9(c) shows a calculated resistivity of the cold sintered $BaTiO_3$ and $BaTiO_3$-PTFE composites as function of the electric field. The polymer distributed in the grain boundary acts as a blocking interface and would limit all types of conduction of both electronic and ionic species.

4. Summary and conclusions

We have been able to fabricate high-density $BaTiO_3$-PTFE composites under the CSP. We found that the importance of selection of starting powder size for the PTFE polymer and ability to disperse successfully through microstructure of the cold sintered composites. The serial connectivity of the $BaTiO_3$-PTFE composites led to lower the overall relative permittivity. This indicates to flatten an anomaly of the relative permittivity and lower the dielectric loss over a broad temperature range. The addition of the PTFE polymer increased the resistivity and suppressed the non-linear *J–E* behavior of the cold sintered materials. The cold sintered composites showed an Ohmic dependence with a much superior resistivity. We fitted the RT permittivity to the general mixing law in order to demonstrate to control more uniform dispersion of the PTFE volume fraction through the microstructure of the composites. We need ideally an exponent $n \sim 0$ which corresponds to an equal weighting of series and parallel connectivity. With the lower n in $BaTiO_3$-200 nm PTFE we can see that it was more dispersed towards this ideal than $BaTiO_3$-3 μm PTFE.

Acknowledgments

The authors would like to acknowledge the staff of Material Characterization Lab at the Pennsylvania State University for electrical characterizations. TN would also like to thank TAIYO YUDEN CO., Ltd. for the visiting scientist scholarship, and CAR would like to thank partial support from NSF_FMSG (2134643).

1) H. Guo, J. Guo, A. Baker, K. Shiratsuyu, and C. A. Randall, ACS Appl. Mater. Interfaces **8**, 20909 (2016).
2) K. Tsuji, A. Ndayishimiye, S. Lowum, R. Floyd, K. Wang, M. Wetherington, J.-P. Maria, and C. A. Randall, J. Eur. Ceram. Soc. **40**, 1280 (2020).
3) T. Sada, K. Tsuji, A. Ndayishimiye, Z. Fan, Y. Fujioka, and C. A. Randall, J. Eur. Ceram. Soc. **41**, 409 (2021).
4) T. Sada, K. Tsuji, A. Ndayishimiye, Z. Fan, Y. Fujioka, and C. A. Randall, J. Appl. Phys. **128**, 084103 (2020).
5) T. Sada, K. Tsuji, A. Ndayishimiye, Z. Fan, Y. Fujioka, and C. A. Randall, Adv. Mater. Interfaces **8**, 2100963 (2021).
6) S. Funahashi, J. Guo, H. Guo, K. Wang, A. Baker, K. Shiratsuyu, and C. A. Randall, J. Am. Ceram. Soc. **100**, 546 (2017).
7) X. Kang, R. Floyd, S. Lowum, M. Cabral, E. Dickey, and J.-P. Maria, J. Am. Ceram. Soc. **102**, 4459 (2019).
8) A. V. Smirnov, M. V. Kornyushin, A. A. Kholodkova, S. A. Melnikov, A. D. Stepanov, E. V. Fesik, V. V. Mnatsakanyan, A. Smirnov, and Y. D. Ivakin, Materials **16**, 408 (2023).
9) J. Gonzalez-Julian, K. Neuhaus, M. Bernemann, J. Pereira da Silva, A. Laptev, M. Bram, and O. Guillon, Acta Mater. **144**, 116 (2018).
10) Y. D. Ivakin, A. V. Smirnov, A. Y. Kurmysheva, A. N. Kharlanov, N. W. Solís Pinargote, A. Smirnov, and S. N. Grigoriev, Materials **14**, 6680 (2021).
11) A. V. Smirnov, M. V. Kornyushin, A. A. Kholodkova, S. A. Melnikov, A. D. Stepanov, E. V. Fesik, and Y. D. Ivakin, Inorganics **10**, 197 (2022).
12) J. Guo, H. Guo, D. S. B. Heidary, S. Funahashi, and C. A. Randall, J. Eur. Ceram. Soc. **37**, 1529 (2017).
13) D. S. B. Heidary, J. Guo, J.-H. Seo, H. Guo, R. Rajagopalan, and C. A. Randall, , Jpn. J. Appl. Phys. **57**, 025702 (2018).
14) Y. Zhao, S. S. Berbano, L. Gao, K. Wang, J. Guo, K. Tsuji, J. Wang, and C. A. Randall, J. Eur. Ceram. Soc. **39**, 1257 (2019).
15) S. H. Bang, T. H. De Beauvoir, and C. A. Randall, J. Eur. Ceram. Soc. **39**, 1230 (2019).
16) J. Guo, A. L. Baker, H. Guo, M. T. Lanagan, and C. A. Randall, J. Am. Ceram. Soc. **100**, 669 (2017).
17) J. Guo, S. S. Berbano, H. Guo, A. L. Baker, M. T. Lanagan, and C. A. Randall, Adv. Funct. Mater. **26**, 7115 (2016).
18) S. S. Berbano, J. Guo, H. Guo, M. T. Lanagan, and C. A. Randall, J. Am. Ceram. Soc. **100**, 2123 (2017).
19) K. Takashima, Y. Iwazaki, and C. A. Randall, Jpn. J. Appl. Phys. **60**, 126505 (2021).
20) W. Lee, C. K. Lyon, J.-H. Seo, R. Lopez-Hallman, Y. Leng, C.-Y. Wang, M. A. Hickner, C. A. Randall, and E. D. Gomez, Adv. Funct. Mater. **29**, 1807872 (2019).
21) Z. Grady, A. Ndayishimiye, and C. A. Randall, J. Mater. Chem. A **9**, 22002 (2021).
22) K. Tsuji, Z. Fan, S. H. Bang, S. Dursun, S. T. McKinstry, and C. A. Randall, J. Eur. Ceram. Soc. **42**, 105 (2022).
23) B. Deng et al., J. Am. Ceram. Soc. **105**, 461 (2022).
24) K. Nakagawa, M. Iwasaki, Z. Fan, J. I. Roscow, and C. A. Randall, J. Eur. Ceram. Soc. **43**, 4015 (2023).
25) F. Bouville and A. Studart, Nat. Commun. **8**, 14655 (2017).
26) F. Renard, D. Bernard, X. Thibault, and E. Boller, Geophys. Res. Lett. **31**, L07607 (2004).
27) A. Ndayishimiye et al., J. Eur. Ceram. Soc. **40**, 1312 (2020).
28) T. Sada, A. Ndayishimiye, Z. Fan, Y. Fujioka, and C. A. Randall, J. Appl. Phys. **29**, 184102 (2021).
29) J. Guo, B. Legum, B. Anasori, K. Wang, P. Lelyukh, Y. Gogotsi, and C. A. Randall, Adv. Mater. **30**, 1801846 (2018).
30) T. H. De Beauvoir, S. Dursun, L. Gao, and C. A. Randall, ACS Appl. Electron. Mater. **1**, 1198 (2019).
31) J. Guo, N. Pfeiffenberger, A. Beese, A. Rhoades, L. Gao, A. Baker, K. Wang, A. Bolvari, and C. A. Randall, ACS Appl. Nano Mater. **1**, 3837 (2018).
32) L. E. Cross, Ferroelectric Ceramics: Tailoring Properties for Specific Applications, 1993, p. 1 10.1007/978-3-0348-7551-6_1.
33) K. Werner, Solid State Phys. **4**, 1 (1957).
34) V. Buscaglia and C. A. Randall, J. Eur. Ceram. Soc. **40**, 3744 (2020).
35) A. V. Polotai, A. V. Ragulya, and C. A. Randall, Ferroelectrics **228**, 93 (2003).
36) T. Hoshina, T. Furuta, Y. Kigoshi, S. Hatta, N. Horiuchi, H. Takeda, and T. Tsurumi, Jpn. J. Appl. Phys. **49**, 09MC02 (2010).
37) H. Kishi, Y. Mizuno, and H. Chazono, Jpn. J. Appl. Phys. **42**, 1 (2003).
38) H. Chazono and H. Kishi, Jpn. J. Appl. Phys. **40**, 5624 (2001).
39) N. G. Devaraju, E. S. Kim, and B. I. Lee, Microelectron. Eng. **82**, 71 (2005).
40) S. D. Cho, S. Y. Lee, J. G. Hyun, and K. W. Paik, J. Mater. Sci.: Mater. Electron. **16**, 77 (2005).
41) M. E. Hossain, S. Y. Liu, S. O'Brien, and J. Li, Acta Mech. **225**, 1197 (2014).
42) H. S. Potdar, S. B. Deshpande, and S. K. Date, J. Am. Ceram. Soc. **79**, 2795 (1996).
43) J. L. Rehspringer and J. C. Bernier, MRS Online Proc. Library **72**, 67 (1986).
44) T. Kanata, T. Yoshikawa, and K. Kubota, Solid State Commun. **62**, 765 (1987).

45) W. Zhong, P. Zhang, Y. Wang, and T. Ren, Ferroelectrics **160**, 55 (1994).
46) L. Curecheriu, M. Buscaglia, V. Buscaglia, Z. Zhao, and L. Mitoseriu, Appl. Phys. Lett. **97**, 242909 (2010).
47) J. Guo, X. Zhao, T. Herisson De Beauvoir, J.-H. Seo, S. S. Berbano, A. L. Baker, C. Azina, and C. A. Randall, Adv. Funct. Mater. **28**, 1801724 (2018).
48) Y. Wu, X. Zhao, F. Li, and Z. Fan, J. Electroceram. **11**, 227 (2003).
49) A. H. Sihvola, Subsurface Sensing Technol. Appl. **1**, 393 (2000).
50) E. Tuncer, Y. V. Serdyuk, and S. M. Gubanski, IEEE Trans. Dielectr. Electr. Insul. **9**, 809 (2002).
51) J. F. Scott, *Ferroelectric Memories* (Springer, Heidelberg, 2000), Vol. 5, p. 107, 10.1007/978-3-662-04307-3_5.
52) H. Chazono and T. Hagiwara, Int. J. Appl. Ceram. Technol. **2**, 45 (2005).
53) K. Morita, Y. Mizuno, H. Chazono, H. Kishi, G. Y. Yang, W. E. Liu, E. C. Dickey, and C. A. Randall, Jpn. J. Appl. Phys. **46**, 2984 (2007).